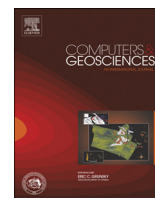




ELSEVIER

Contents lists available at ScienceDirect

Computers & Geosciences

journal homepage: www.elsevier.com/locate/cageo

Two- and three-dimensional Direct Numerical Simulation of particle-laden gravity currents

L.F.R. Espath^a, L.C. Pinto^a, S. Laizet^b, J.H. Silvestrini^{a,*}^a Faculdade de Engenharia, Pontifícia Universidade Católica do Rio Grande do Sul, Av. Ipiranga 6681, 90619-900 Porto Alegre, RS, Brazil^b Turbulence, Mixing and Flow Control Group, Department of Aeronautics, Imperial College London, London SW7 2BY, United Kingdom

ARTICLE INFO

Article history:

Received 10 July 2013

Received in revised form

10 October 2013

Accepted 12 October 2013

Available online 21 October 2013

Keywords:

Particle-laden gravity current

Energy budget

Deposition of particles

Direct Numerical Simulation

ABSTRACT

In this numerical study, we are interested in the prediction of a mono-disperse dilute suspension particle-laden flow in the typical lock-exchange configuration. The main originality of this work is that the deposition of particles is taken into account for high Reynolds numbers up to 10 000, similar to the experimental ones. Unprecedented two- and three-dimensional Direct Numerical Simulations (DNS) are undertaken with the objective to investigate the main features of the flow such as the temporal evolution of the front location, the sedimentation rate, the resulting streamwise deposit profiles, the wall shear velocity as well as the complete energy budget calculated without any approximations for the first time. It is found that the Reynolds number can influence the development of the current front. Comparisons between the 2D and 3D simulations for various Reynolds numbers allow us to assess which quantities of interest for the geoscientist could be evaluated quickly with a 2D simulation. We find that a 2D simulation is not able to predict accurately the previously enumerated features obtained in a 3D simulation, with maybe the exception of the sedimentation rate for which a qualitative agreement can be found.

© 2013 Elsevier Ltd. All rights reserved.

1. Introduction

Gravity currents are very common in nature, either in atmosphere due to sea-breeze fronts, in mountain avalanches of air-borne snow or debris flows, or in the ocean due to turbidity currents and river plumes (Simpson, 1982). It is clear that the understanding of the physical mechanism associated with these currents as well as the correct prediction of their main features is of great importance for practical and theoretical purposes.

In this numerical study, we focus on particle-laden hyperpycnal flows (with negative-buoyancy) where dynamics can play a central role in the formation of hydrocarbon reservoirs (Meiburg and Kneller, 2009). Moreover, these particle-laden gravity currents are often extremely dangerous for the stability of submarine structures placed at the sea-floor like pipelines or submarines cables (Zakeri et al., 2008; Nisbet and Piper, 1998). We focus on the prediction of a mono-disperse dilute suspension particle-laden flow in the typical lock-exchange configuration where the deposition of particles is taken into account. We consider only flat surfaces using DNS (Direct Numerical Simulation). Our approach takes into account the possibility of particles deposition but ignores erosion and/or re-suspension. Note

that in dilute suspensions, the particle volume fraction is considered relatively small, typically well below 1%.

Previous results for this kind of flows were obtained in laboratory experiments (de Rooij and Dalziel, 2001; Gladstone et al., 1998), using simplified theoretical models (Rottman and Simpson, 1983; Bonnecaze et al., 1993), or by numerical simulations (Necker et al., 2002, 2005; Nash-Azadani et al., 2011) for relatively small Reynolds numbers. It was shown that deposition, boundary conditions, initial conditions associated with the lock configuration, and particle sizes can have a strong influence on the main characteristics of such flows. Cantero et al. (2008) already performed DNS of planar gravity current in the Boussinesq limit for Reynolds number equal to 8950 and 15 000. However, the simulations were performed for density-driven gravity currents (no particle deposition) not for particle-laden gravity currents like in the present work. The authors carried out a detailed investigation about the effect of three-dimensionality and turbulent structures and their influence on the flow dynamics but only for gravity currents with no deposition.

One of the principal objectives of this numerical study is to investigate the complete energy budget in particle-laden gravity currents for various Reynolds numbers with a comparison between two- and three-dimensional simulations. The main features of the flow are related with the temporal evolution of the front location as well as the suspended sediment mass, sedimentation rate, the resulting streamwise deposit profiles.

* Corresponding author. Tel.: +55 51 3353 8307; fax: +55 51 3320 3525.
E-mail address: jorgehs@puccs.br (J.H. Silvestrini).

Concerning the complete energy budget of the flow, each term is evaluated without simplification assumptions, with the potential energy and kinetic energy as well as the dissipation related to the potential and kinetic energy variation. Within this framework, an excellent estimation should be obtained for the potential energy and kinetic energy and for the dissipation, with the preservation of the total energy inside the computational domain.

The organisation of this paper is as follows. In [Section 2](#), we present the flow configuration and governing equation. The energy budget is explained in [Section 3](#) while the numerical parameters and flow parameters of each simulation are detailed in [Section 4](#). Some suggestive flow visualisations are presented and discussed in [Section 5](#). Then, in order to better understand the underlying properties of each flow, some temporal results are presented in [Section 6](#), followed by a conclusion in [Section 7](#).

2. Flow configuration and governing equations

The well-known lock-exchange flow configuration is used in this numerical work (see [Fig. 1](#)) where uniformly suspended particle sediments are enclosed in a small portion of the dimension domain $L_{1b} \times L_{2b} \times L_{3b}$ separated by a gate with clear fluid. When the gate is removed the particle–fluid mixture flows due to gravity with a mutual inverse interaction between the “heavy” particle–mixture flow and the “light” clear fluid. The motion is understood as the transformation from potential energy to kinetic energy. We assume a dilute suspension of single diameter particles and we do not take into account the influence of particle inertia and/or particle–particle interaction. It should be noted that the concentration affect the mixture viscosity, however this effect is neglected.

With the restriction imposed by the dilute suspension approach, this flow can be evaluated numerically by solving the incompressible Navier–Stokes and a scalar transport equation under the Boussinesq approximation. Also, these assumptions allow to relate the particle diameter with the settling velocity. To make these equations dimensionless, half of the box height is chosen ([Fig. 1](#)) as the characteristic length scale h and the buoyancy velocity u_b is chosen as the velocity scale. The buoyancy velocity is related to the reduced gravitational acceleration $u_b = \sqrt{g'h}$ where $g' = g(\rho_p - \rho_0)c_i/\rho_0$. The particle and clear fluid densities are ρ_p and ρ_0 , respectively, with g being the gravitational acceleration and c_i the initial volume fraction of the particles in the lock. When introducing the velocity and length scales two dimensionless numbers appear in the equations: the Reynolds number defined as $Re = u_b h/\nu$ where ν is the kinematic viscosity of the fluid, and the Schmidt number $Sc = \nu/k$, where k is the mass diffusivity of the particle–fluid mixture. All other parameters and variables are made dimensionless using c_i , h or/and u_b . Thus, the dimensionless form for the governing equation and scalar transport equation are

$$\frac{\partial \mathbf{u}}{\partial t} + \mathbf{u} \cdot \nabla \mathbf{u} = \frac{2}{Re} \mathbf{div}(\mathbf{s}) - \nabla p + c \mathbf{e}^g \quad (1a)$$

$$\mathbf{div}(\mathbf{u}) = 0 \quad (1b)$$

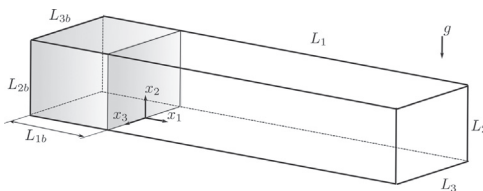


Fig. 1. Schematic view of the initial configuration of the lock-exchange flow problem.

$$\frac{\partial c}{\partial t} + (\mathbf{u} + u_s \mathbf{e}^g) \nabla c = \frac{1}{Sc Re} \nabla^2 c \quad (1c)$$

where $\mathbf{e}^g = (0, -1, 0)$ is the unit vector in gravity direction and the non-dimensional quantities \mathbf{u} , p , c , \mathbf{s} represent the fluid velocity, pressure, particle concentration, and strain rate tensor fields, respectively. The particle settling velocity u_s is related to the particle diameter by the Stokes settling velocity law ([Julien, 2010](#)).

For the initial condition, a weak perturbation is imposed on the velocity field at the lock-exchange interface in order to mimic the disturbances introduced in the flow when the mixture is released. Free-slip boundary conditions are imposed for the velocity field in the streamwise and spanwise directions while no-slip boundary conditions are used in the vertical direction. For the scalar field, no-flux conditions are used in the streamwise and spanwise directions and in the vertical direction at the top of the domain. In order to take into account the particles deposition in the vertical direction at the bottom of the domain, the following outflow boundary condition is used:

$$\frac{\partial c}{\partial t} + u_s \mathbf{e}_z^g \frac{\partial c}{\partial x_2} = 0 \quad (2)$$

It allows particles to leave the computational domain mimicking a deposition process. It should be noticed that no re-suspension is allowed, as well as no erosion.

3. Energy budget of the flow

Following previous studies ([Winters et al., 1995](#); [Necker et al., 2005](#)), we present in this section a framework for the analysis of the energy budget. It is possible to better understand particle-laden gravity currents by investigating the temporal evolution of the potential energy and the kinetic energy. The main difference between density-driven gravity currents and particle-laden gravity currents is that dissipation occurs not only at the macroscopic scale with the strain rate but also at the microscale scale around each particles.

In order to accurately investigate the temporal evolution of the different energy components, we consider the full budget equation for the kinetic energy. A similar approach, with simplifying assumptions, can be found in [Necker et al. \(2005\)](#). The main difference between the present work and the work of [Necker et al. \(2005\)](#) is that we compute the exact energy equation (8) without any assumptions over the dissipation terms.

The energy budget for an incompressible flow with particle concentration in the dilute suspension approach can be extracted from the governing equations and scalar transport equation. The total energy can be split into the kinetic energy and potential energy, and distinguish the dissipation associated to the strain rate in the macroscopic advective motion and the dissipation that occurs in the microscopic Stokes flows around the particles.

The time derivative of the kinetic energy equation is derived from the inner product between the momentum equation (1a) with \mathbf{u} and is expressed as

$$D \left(\frac{1}{2} \mathbf{u} \cdot \mathbf{u} \right) \frac{1}{Dt} = -\mathbf{div}(p\mathbf{u}) + \frac{2}{Re} \mathbf{div}(\mathbf{s} \cdot \mathbf{u}) - \frac{2}{Re} \mathbf{s} : \mathbf{s} - u_2 c \quad (3)$$

where $D(\cdot)/Dt$ is the material derivative. Integrating Eq. (3) over the entire domain Ω gives

$$\frac{dk}{dt} = - \int_{\Omega} \frac{2}{Re} \mathbf{s} : \mathbf{s} d\Omega - \int_{\Omega} u_2 c d\Omega \quad (4)$$

where Ω represents the entire computational domain and $k(t) = \int_{\Omega} \frac{1}{2} \mathbf{u} \cdot \mathbf{u} d\Omega$. Note that any integral of a divergence field over the domain is zero because there is no transport across the boundaries.

For the potential energy, that can be expressed as

$$E_p(t) = \int_{\Omega} cx_2 d\Omega \quad (5)$$

we can define its variation in time by using the multiplication of the transport equation of the particle concentration (1c) by x_2 :

$$\frac{Dc}{Dt}x_2 = \frac{1}{Sc Re}x_2\nabla^2c + x_2u_s\frac{\partial c}{\partial x_2} \quad (6)$$

By integrating over the domain computational domain Ω and using the chain rule, we obtain

$$\frac{dE_p}{dt} = \int_{\Omega} \frac{D(cx_2)}{Dt} d\Omega = \int_{\Omega} \left(\frac{1}{Sc Re}x_2\nabla^2c + x_2u_s\frac{\partial c}{\partial x_2} \right) d\Omega + \int_{\Omega} u_2c d\Omega \quad (7)$$

From Eqs. (4) and (7) the exact dissipation terms can be defined as

$$\begin{aligned} \frac{d(k+E_p)}{dt} &= - \int_{\Omega} \frac{2}{Re} \mathbf{s} : \mathbf{s} d\Omega + \int_{\Omega} \left(\frac{1}{Sc Re}x_2\nabla^2c + x_2u_s\frac{\partial c}{\partial x_2} \right) d\Omega \\ &= -\varepsilon - \varepsilon_s \end{aligned} \quad (8)$$

where ε is associated to the turbulent dissipation while ε_s is the dissipation associated with loss of energy due to suspended particles.

In order to study the temporal evolution of ε and ε_s , we can define E_d and E_s as the time integrals of the dissipation components ε and ε_s with

$$E_d(t) = \int_0^t \varepsilon(\tau) d\tau \quad (9)$$

$$E_s(t) = \int_0^t \varepsilon_s(\tau) d\tau \quad (10)$$

It is worth noticing that Necker et al. (2002, 2005) estimated E_s as

$$E_s(t) = u_s \int_0^t \int_{\Omega} c d\Omega d\tau \quad (11)$$

meaning that this dissipation term is defined as a function of the suspended material.

4. Numerical method and parameters

In order to solve numerically the incompressible Navier–Stokes equations and the transport scalar equation (1c), the in-house code `Incompact3d`¹ is used. It is based on compact sixth-order finite difference schemes for spatial differentiation and a third-order Adams–Bashforth scheme for time integration. To treat the incompressibility condition, a fractional step method requires to solve a Poisson equation. This equation is fully solved in spectral space via the use of relevant 3D Fast Fourier Transforms. More information about the code can be found in Laizet and Lamballais (2009). For the 3D simulations, the parallel version of `Incompact3d` based on a powerful 2D domain decomposition is used. More details about this 2D domain decomposition can be found in Laizet and Li (2011).

The number of mesh nodes and the size of the simulations have been carefully chosen in order to solve the smallest scales of the flow and are presented in Table 1. We consider a subdomain of $(L_{1b}, L_{2b}, L_{3b}) = (1, 2, 2)$ to define the box containing the particle–fluid mixture. The settling velocity is set to $u_s = 0.02$, corresponding to a middle silt, while the Schmidt number is fixed to $Sc = 1$. These values were used in Necker et al. (2002), allowing direct comparisons. All the simulations were run for a non-dimensional time of

Table 1
Summary of numerical parameters.

Re	L_1, L_2, L_3	n_1, n_2, n_3	Δt
2236			
2D	18, 2	1441, 221	1×10^{-3}
3D	18, 2, 2	1441, 221, 201	6.024×10^{-4}
5000			
2D	18, 2	1537, 257	5×10^{-4}
3D	18, 2, 2	1537, 257, 257	5×10^{-4}
10 000			
2D	18, 2	2305, 513	3×10^{-4}
3D	18, 2, 2	2305, 513, 385	3×10^{-4}

$t = 60$ except for the $Re = 10\,000$ which was stopped at $t = 32$ in order to limit the computational effort. The perturbation added to the initial velocity field is adjusted in order to get an initial kinetic energy equal to $\approx 1\%$ of the initial potential energy.

The Reynolds number 2236 case is similar to the numerical work of Necker et al. (2002) in order to undertake comparisons. The only difference lies in the way the weak perturbation is added in the initial condition for the velocity field. Finally, the $Re = 10\,000$ case is very close to the experimental configuration of de Rooij and Dalziel (2001) and was never attempted before by DNS in 3D.

5. Instantaneous visualisations

The sudden release of the particle–fluid mixture along the left wall leads to the streamwise evolution of the gravity current into the clear fluid. Due to the small amount of kinetic energy at $t = 0$, this motion is initially two dimensional for $Re = 2236$ then further downstream three-dimensional structures can be observed at the head and at the tail of the current as shown in Fig. 2 (left). For the $Re = 10\,000$ presented in Fig. 2 (right), the two-dimensional behaviour is not present at $t = 2$ suggesting that there is a strong effect of the Reynolds number on the flow evolution. For both cases, it can be seen that for $t = 14$ the gravity current develops a high 3D turbulence with intense streamwise vortices. It is confirmed by the Q -criterion visualisations in Fig. 3 for the three Reynolds numbers at $t = 20$. We can clearly see the higher level of turbulence with smaller and very intense structures for the $Re = 10\,000$ simulation by comparison with the lower Re simulations, confirming the influence of the Reynolds number in such flows.

At the bottom wall of the channel, increasing spanwise motions are responsible for the well known lobe-and-cleft structures that are developing at the current front location. In Fig. 4, the velocity gradient at the wall, computed as $\sqrt{(\partial u_1/\partial x_2)^2 + (\partial u_3/\partial x_2)^2}|_{x_2=0}$, is shown for the 3D cases for $t = 8$. It can be seen that the front structure looks like a “dental radiography”, corresponding to zones of high shear velocity, the lobes, alternating with regions of low shear velocity, the clefts. The influence of the Reynolds number on the wall shear velocity is quite important with thinner and longer structures at the front of the current and more complex patterns in the middle and at the tail of the current when the Reynolds number is increased.

The origin of the lobe-and-cleft patterns has been identified experimentally (Simpson, 1972, 1999; Britter and Simpson, 1978): they are created by the fast velocity of the front overstepping the clear fluid at the lower wall of the domain. Those complex structures were observed in many experiments (Simpson, 1982) and more recently in the density-driven current simulations (without suspended particles) of Härtel et al. (2000a) and Cantero et al. (2008) and the particle-laden simulations of Necker et al. (2002). At $t = 8$ the structure of the gravity current front can be seen in detail through the visualisation of the concentration field as shown on the left side of Fig. 5. The isovalue chosen is $c = 0.25$. A cross

¹ This open source code is now available at <http://code.google.com/p/incompact3d/>.

section of the Q -criterion for the selected vertical planes at a distance $0.33 h$ just behind the location of the front is shown at the right side of the same picture. The lobe-and-cleft patterns can be well identified with regions with a high strain rate (indicated in blue, negative Q -criterion), the clefts, along with the regions between two streamwise vortices (positive values of Q -criterion corresponding to a high rotation rate, indicated in red), the lobes. The figure also shows how the streamwise vortices become thinner and thinner and more intense when the Reynolds number is increased. Fig. 5 suggests that the situation is far more complex for the $Re=10\,000$ case where the lobe-and-cleft patterns have a more complex structure, with regions of high strain rate and of high rotation rate on top of each other.

In Fig. 6 snapshots of the concentration field are shown at $t=20$ for the 2D cases (left) and for the $x_3=0$ middle-plane for 3D (right) simulations for the three Re numbers considered. Some important discrepancies between the 2D and 3D simulations concerning mainly the front location, the development of the Kelvin–Helmholtz instability and the resulting vorticity structures can be seen. Furthermore, due to particle settling, high levels of particle concentration are located near the wall for the 3D case whereas for the 2D cases it can be seen that high levels of concentration are trapped by the vorticity located at the middle and tail of the current. This result denotes that the particle mass should remain suspended for longer time for the 2D case. The particle concentration fields for the 3D simulations also show that when the Reynolds number is increased, the suspended mass is decreased. This point will be addressed in the following section.

6. Temporal results

In this section, the temporal evolution for the front location, suspended particles mass, sedimentation rate, deposit profiles at the bottom of the computational domain and energy budget of the flow are compared with the numerical predictions obtained by Necker et al. (2002) for $Re=2236$ and with the experimental data of de Rooij and Dalziel (2001) for $Re=10\,000$.

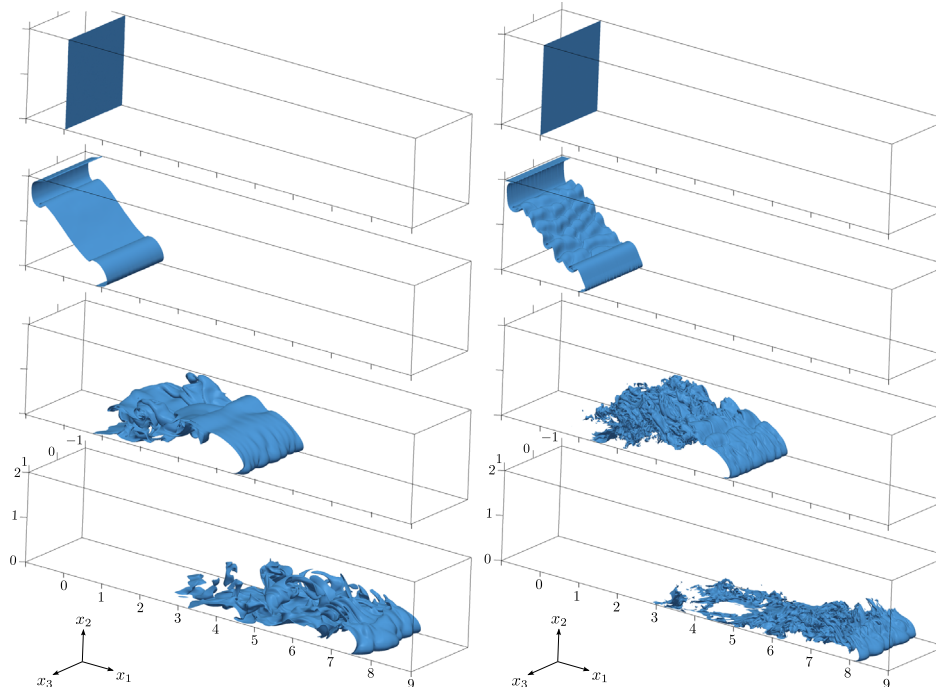


Fig. 2. Interface evolution between clear fluid and particle-fluid ($t=0, 2, 8, 14$ from top to bottom) for a concentration $c=0.25$ (Left for $Re=2236$ and right for $Re=10\,000$).

Fig. 7 shows the time evolution of the front location, x_f , corresponding to the first streamwise location where the streamwise component of the concentration gradient (after an average in the spanwise direction) is non-zero when starting from the end of the computational domain. The figure also shows the suspended mass normalized by the initial suspended mass m_p/m_{p_0} with

$$m_p(t) = \int_{\Omega} c \, dV \quad (12)$$

It can be observed that the particle-laden gravity current has a constant front velocity until time $t \approx 10$, similar to density-driven

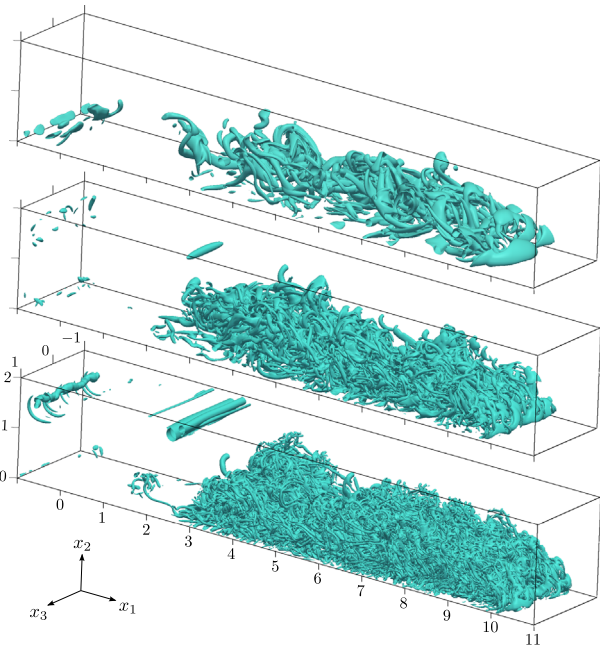


Fig. 3. Turbulent structure of the gravity currents by isosurfaces of Q -criterion (for the isovalue $Q=1$) for $Re=2236, 5000, 10\,000$ (from top to bottom) at $t=20$.

current without particles as shown in Härtel et al. (2000b). After $t \approx 10$ the front velocity deviates from the straight line with a substantial decrease due to particles settling. It seems that the suspended particles mass m_p is deviating earlier when the Reynolds number is decreased for the 2D and 3D cases. Our data compare well with the numerical data of Necker et al. (2002) for $Re=2236$. The small differences can be related to the perturbations added as initial condition on the velocity field. At the early state of a simulation, the gravity current in the lock-exchange configuration is transitioning from a laminar state inside the lock to a fully turbulent state. Therefore, it is strongly dependent on initial conditions and Reynolds number as pointed out by Necker et al. (2002). Nevertheless, there is a clear tendency for an increasing front velocity when the Reynolds number is increased. This trend is more pronounced for the 3D cases, as already observed in Fig. 6. Concerning the suspended mass, the value obtained at the end of the simulation is quite different between the 2D cases and 3D cases with values lower than 5% obtained for the 3D cases and values higher than 10% for the 2D cases. Furthermore, a faster decrease for the suspended mass for the 3D simulations can be noticed between $t \approx 10$ and $t \approx 40$ for high Reynolds numbers.

Fig. 8 shows the sedimentation rate $\dot{m}_s(t)$ as a function of time for the 2D and 3D configurations with

$$\dot{m}_s = \frac{1}{L_1 L_3} \int_0^{L_1} \int_0^{L_3} c_w(x_1, x_3, t) u_s dx_3 dx_1, \quad (13)$$

where c_w is the concentration at the wall.

The initial value for $\dot{m}_s(t)$ is 0.02, corresponding to the settling velocity. In this figure, it can be seen that $\dot{m}_s(t)$ is slowly increasing

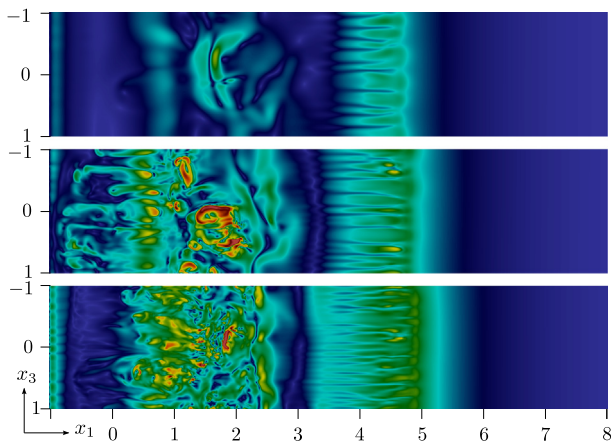


Fig. 4. Velocity gradient at the wall for the 3D simulations at $t=8$ for $Re=2236$, 5000, 10 000 (from top to bottom). Same colour distribution for all pictures (blue corresponds to 0 and red to 15). (For interpretation of the references to colour in this figure caption, the reader is referred to the web version of this paper.)

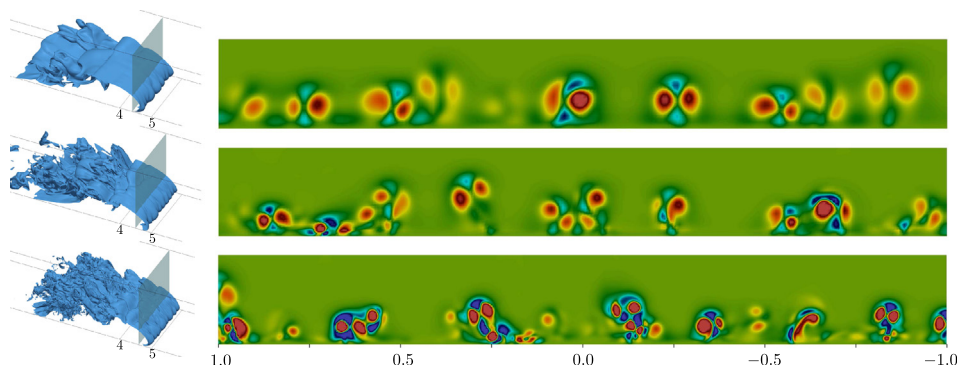


Fig. 5. Structure of the front by isosurface for $c=0.25$ (left) and Q -criterion with an isovalue ranging from $-25 < Q < 25$ (right) for $Re=2236$, 5000, 10 000 (from top to bottom) at $t=8$.

for all cases up to $t \approx 10$ at a slow rate of about $t^{0.5}$, in agreement with Necker et al. (2002). It means that in the early stage of the simulations, there is very little mixing for the suspended particles with the clear fluid with limited turbulence motions occurring at the head of the front, in agreement with the visualisations in Fig. 2 at $t=14$. This was also observed by Ungarish and Huppert (1998) with the concept of “laminar settling process”. The figure shows a peak value around $t \approx 15$ independent of the Reynolds number. When this happens, $\approx 50\%$ of the suspended particles are already settled, as shown in Fig. 7. After $t \approx 15$, the sedimentation rate is suddenly decreasing at a rate of about $t^{-2.5}$ when the front velocity is slowing down, with a fully turbulent head of the front. It seems that there is only a limited effect of the Reynolds number on the sedimentation rate in 2D whereas in 3D the sedimentation rate is lower for $Re=5000$ and $Re=10\,000$ by comparison with $Re=2236$.

Another global quantity of extremely importance for practical implications is the streamwise deposit of sediment particles computed as

$$D_t(x_1, t) = \int_0^t \langle c_w(x_1, \tau) \rangle_{x_3} u_s d\tau, \quad (14)$$

where $\langle \cdot \rangle_{x_3}$ indicated a mean value in the x_3 direction (only valid for the 3D cases). Fig. 9 shows this quantity in function of the streamwise coordinate x_1 . The deposit is normalized with the deposit for the final time $t=60$. For the 2D (left of Fig. 9) and the 3D cases (right of Fig. 9), the selected times are $t=7.3, 11, 60$. Note that the 3D DNS for $Re=10\,000$ was stopped at $t=32$ to limit the computational effort so data are not available for this case. However, the present results may be compared both with the numerical data of Necker et al. (2002) and the experimental data of de Rooij and Dalziel (2001). Despite the difference in terms of Reynolds number, a global agreement between experimental data and numerical results can be seen in this figure, even if 2D simulations seem to overestimate the deposit at the end of the simulation. The left picture of Fig. 9 shows that 2D simulations are giving incorrect prediction for high values of the deposit regardless of the Reynolds number. On the other hand, the 3D results for the Reynolds number 5000 case are very close to the experimental data of de Rooij and Dalziel (2001) both at initial and final times of the simulation. The differences could be attributed to different initial conditions between laboratory experiments and numerical simulations.

As already stated, the temporal evolution of the potential energy and kinetic energy is of fundamental importance for particle-laden gravity currents. Fig. 10 presents the energy budget, with comparisons with the predictions obtained by Necker et al. (2002), for the 2D and 3D cases. The data presented are normalized with E_{T_0} which is defined as the total energy at $t=0$.

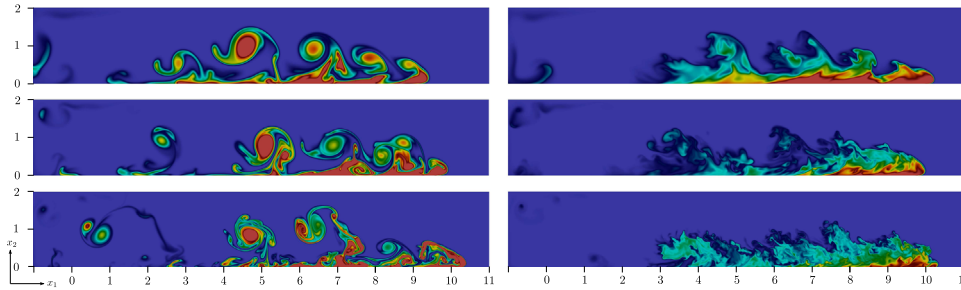


Fig. 6. Particle concentration fields at $t=20$ for $Re=2236, 5000, 10\ 000$ (from top to bottom) for the 2D (left) and the $x_3=0$ middle plane for the 3D (right) configurations. Snapshots taken for $0 < c < 0.3$.

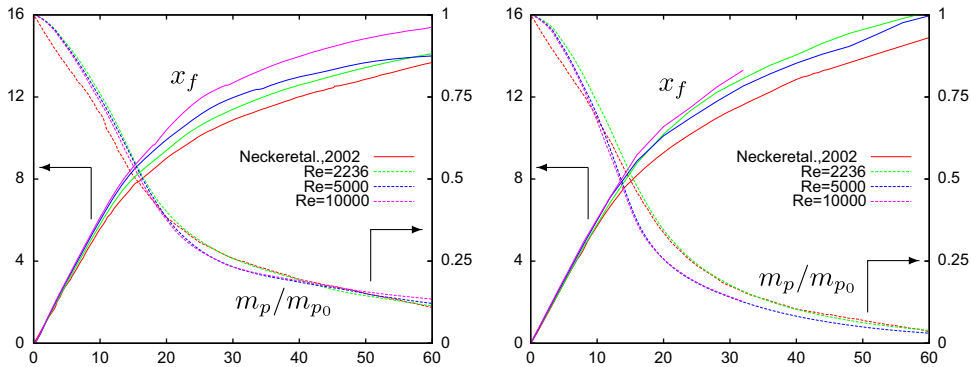


Fig. 7. Front location x_f and suspended particles mass m_p/m_{p0} as a function of time for the 2D (left) and the 3D (right) configurations with comparisons with the numerical data of Necker et al. (2002).

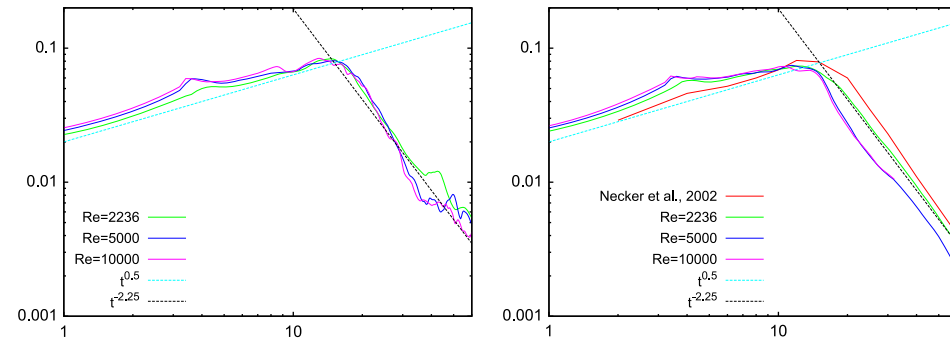


Fig. 8. Sedimentation rate $m_s(t)$ as function of time for the 2D (left) and the 3D (right) configurations, with comparisons with the numerical data of Necker et al. (2002).

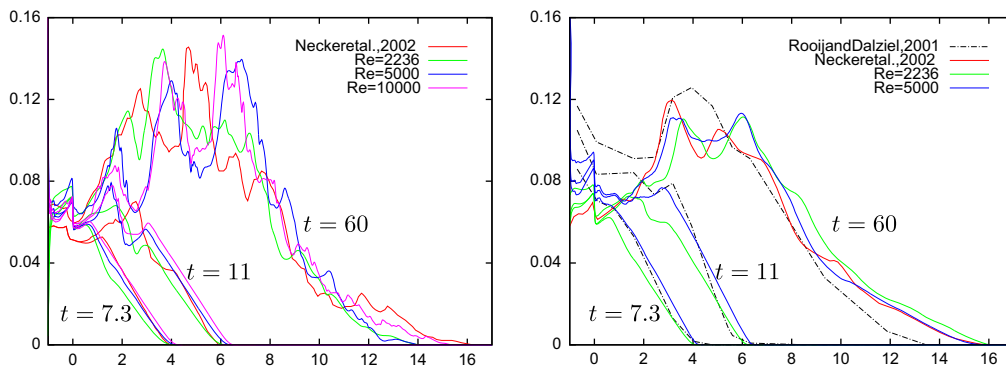


Fig. 9. Deposit profiles for $t=7.3, 11, 60$ for the 2D (left) and the 3D (right) simulations with comparisons with the numerical data of Necker et al. (2002) and the experimental data of de Rooij and Dalziel (2001).

The overall agreement for the Reynolds number 2236 case with the data of Necker et al. (2002) is reasonably good. As already mentioned before, it is important to notice that difference observed between our predictions with those obtained by Necker et al. (2002) can be related not only to the initial condition but also to the

formulation of the energy budget. Concerning the initial condition, a parametric study was carried out by Necker et al. (2002) with the observation that the flow is highly dependent of the initial condition, especially for E_s . For the energy budget, the evaluation of micro-dissipation carried out by Necker et al. (2002) was done with

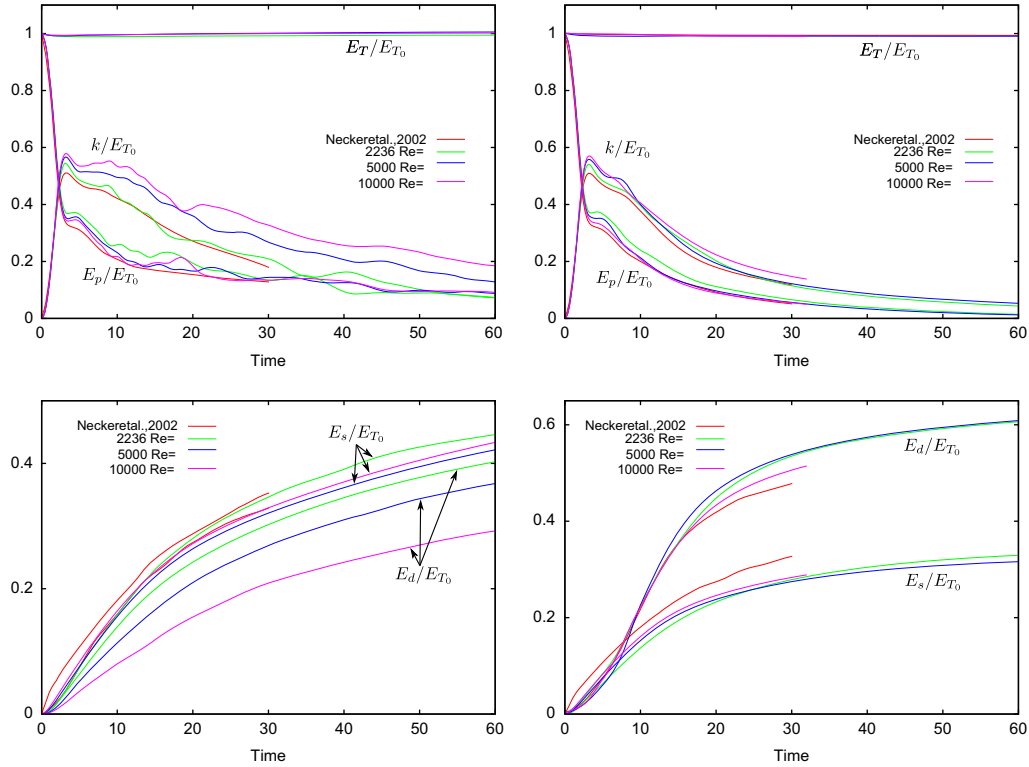


Fig. 10. Time history of the kinetic and potential energy (top figures), turbulent and particle-settling dissipation (bottom figures) for the 2D cases (left figures) and 3D cases (right figures) for the three different Reynolds number with comparisons with the numerical data of Necker et al. (2002).

simplifying assumptions, and if we compare this micro-dissipation with the exact evaluation, we can observe that the simplified dissipation is giving an over-estimated value by comparison with the full dissipation. The approach with simplifying assumptions yields to an error of 15%(2D)/18%(3D) for the micro-dissipation term for the $Re=2236$ case. This error represents a difference of about 5%(2D)/6%(3D) for the total energy. Concerning the contribution of each term for the computation of the micro-dissipation, the Laplacian term in Eq. (8) only contributes for 5.4% while the gradient term contributes for about 94.6% in the 2D case. For the 3D case, the Laplacian term contributes for about 6.1% while the gradient term contributes for about 93.9%. These results clearly show the important contribution of the gradient term for the total micro-dissipation. The approach with simplifying assumptions yields to an error of 5%(2D)/7%(3D) in the dissipation term for the $Re=10\,000$ case corresponding to a relatively small error of 2%(2D)/2%(3D) for the total energy. This approach can lead to a good approximation for high Reynolds numbers because of the minor contribution from the Laplacian term in Eq. (8) when compared to the gradient term. It should be noted that the conservation of energy of the system can only be verified with the complete approach without simplifying assumptions.

The first important result here is that $E_T = E_p + k + E_d + E_s$ is constant in our simulations, meaning that the energy is well conserved. Then, it can be seen that at the very early stage of the simulation, there is a very fast drop of the potential energy E_p by about 80% before $t \approx 10$ whereas the kinetic energy is increasing very quickly with a peak for $t \approx 4$ followed by a steady decay, due to the increasing influence of the dissipation that is playing a key role in the flow temporal evolution. At the end of the simulation, the kinetic energy and the potential energy are slowly evolving to zero. As expected, the peak of kinetic energy is increased when the Reynolds number is increased.

For the two dissipation components E_d and E_s we can observe a strong difference between the 2D and 3D cases: The dissipation E_s

related to particle-settling is dominating the dissipation E_d related to the turbulence only in the early stages of the simulation for up to $t \approx 4$ for the 3D cases while for the 2D cases, the dissipation E_s is always more important than the dissipation E_d . The values obtained at the end of the simulation indicate how much of the initial potential energy has been dissipated due to the particles settling and how much has been dissipated due to the turbulence via the strain rate. It should be noticed that there is a strong effect of the Reynolds number on the two dissipation for the 2D and 3D cases. In 3D, there is more dissipation due to the turbulence when the Reynolds number is increased with more small scales structures present in the flow. However, the effect on the dissipation due to particle-settling dissipation is relatively limited for the 3D cases where $\approx 30\%$ of the energy loss is due to E_s . For the 2D cases, the particle-settling dissipation is always dominating the turbulence dissipation as 2D turbulence is obviously quite poor in small structures. Interestingly, there is a strong effect of the Reynolds number on E_s . For $Re=10\,000$, at the end of the simulation, E_s is responsible for $\approx 30\%$ of the energy loss whereas it is responsible for more than 40% for $Re=2236$. It means that for the lower Reynolds number, there is less energy available for the transport and mixing of particle.

7. Conclusion

The main features of a particle-laden gravity current for a dilute suspension in a lock-exchange configuration were examined using the 2D and 3D DNS for various Reynolds numbers. These simulations were performed in order to gain more information of the influence of the Reynolds number on the wall shear velocity, the front structures, the temporal evolution of the front location, the sedimentation rate and the resulting streamwise deposit profiles. The full energy budget was also calculated for the first time with no approximations. Direct comparisons with previous

experimental and numerical works were also performed in order to validate the approach. Good agreements were found with those previous studies.

One of the main findings is that 2D simulations are unable to reproduce the main features of the flow observed in the 3D cases for the Reynolds numbers considered in this study. For instance, 2D simulations are unable to produce the switch for the dissipation related to the turbulence and the one related to the particle-settling, observed at $t \approx 8$ in the 3D simulations. The 2D simulations are also exhibiting a non-realistic particle concentration with very intense patches of concentration along the front, due to strong vortices. Because of this phenomenon, the deposition profiles cannot be correctly predicted in 2D. It seems that the only quantity that can be qualitatively well evaluated in 2D is the sedimentation rate.

The next step is to investigate the turbulence characteristics of the flow, and to focus on the destabilisation mechanisms of the head of the front. In particular, we would like to investigate in great details the streamwise evolution of the lobe-and-cleft patterns. These structures have been reported in several studies, nevertheless, the transitory signature of the lobe-and-cleft patterns has not been yet investigated. Very little is known about the transition from a front with well defined lobe-and-cleft patterns to a turbulent front and about the interaction with the Kelvin–Helmholtz vortices.

Acknowledgements

We would like to thank one of the referees who helped us improving the paper. Present simulations have been carried out at the Pontifical Catholic University of Rio Grande do Sul (PUCRS) High Performance Computing facility LAD. The authors are grateful to Petrobras for supporting this research. JHS acknowledges financial assistance of CNPq.

References

- Bonnecaze, R., Huppert, H., Lister, J., 1993. Particle-driven gravity currents. *J. Fluid Mech.* 250, 339–369.
- Britter, R., Simpson, J., 1978. Experiments on the dynamics of a gravity current head. *J. Fluid Mech.* 88, 223–240.
- Cantero, M., Balachandar, S., Garcia, M., Bock, D., 2008. Turbulent structures in planar gravity currents and their influence on the flow dynamics. *J. Geophys. Res. Oceans* 113, C08018.
- de Rooij, F., Dalziel, S., 2001. Time- and space-resolved measurements of deposition under turbidity currents. *Spec. Publ. Int. Assess. Sediment.* 31, 207–215.
- Gladstone, C., Phillips, J., Sparks, R., 1998. Experiments on bidisperse, constant-volume gravity currents: propagation and sediment deposition. *Sedimentology* 45, 833–843.
- Härtel, C., Carlsson, F., Thunblom, M., 2000a. Analysis and direct numerical simulation of the flow at a gravity-current head, Part 2: The lobe-and-cleft instability. *J. Fluid Mech.* 418, 213–229.
- Härtel, C., Meiburg, E., Necker, F., 2000b. Analysis and direct numerical simulation of the flow at a gravity-current head, Part 1: Flow topology and front speed for slip and no-slip boundaries. *J. Fluid Mech.* 418, 189–212.
- Julien, P., 2010. *Erosion and Sedimentation*. Cambridge University Press.
- Laizet, S., Lamballais, E., 2009. High-order compact schemes for incompressible flows: a simple and efficient method with the quasi-spectral accuracy. *J. Comput. Phys.* 228, 5989–6015.
- Laizet, S., Li, N., 2011. Incompact3d: a powerful tool to tackle turbulence problems with up to $O(10^9)$ computational cores. *Int. J. Numer. Meth. Fl.* 67, 1735–1757.
- Meiburg, E., Kneller, B., 2009. Turbidity currents and their deposits. *Annu. Rev. Fluid Mech.* 42, 135–156.
- Nash-Azadani, M., Hall, B., Meiburg, E., 2011. Polydisperse turbidity currents propagating over complex topography: comparison of experimental and depth-resolved simulation results. *Comput. Geosci.* 53, 141–153.
- Necker, F., Härtel, C., Kleiser, L., Meiburg, E., 2002. High-resolution simulations of particle-driven gravity currents. *Int. J. Multiphase Flow* 28, 279–300.
- Necker, F., Härtel, C., Kleiser, L., Meiburg, E., 2005. Mixing and dissipation in particle-driven gravity currents. *J. Fluid Mech.* 545, 339–372.
- Nisbet, E., Piper, D., 1998. Giant submarine landslides. *Nature* 392, 329–330.
- Rottman, J., Simpson, J., 1983. Gravity currents produced by instantaneous releases of a heavy fluid in a rectangular channel. *J. Fluid Mech.* 135, 95–110.
- Simpson, J., 1972. Effects of the lower boundary on the head of a gravity current. *J. Fluid Mech.* 53 (4), 759–768.
- Simpson, J., 1982. Gravity currents in the laboratory, atmosphere and ocean. *Annu. Rev. Fluid Mech.* 14, 213–234.
- Simpson, J., 1999. *Gravity Currents in the Environment and in the Laboratory*. Cambridge University Press.
- Ungarish, M., Huppert, H., 1998. The effects of rotation on axisymmetric particle-driven gravity currents. *J. Fluid Mech.* 362, 17–51.
- Winters, K., Lombard, P., Riley, J., D'Asaro, E., 1995. Available potential energy and mixing in density-stratified fluids. *J. Fluid Mech.* 289, 115–128.
- Zakeri, A., Hoeg, K., Nadim, F., 2008. Submarine debris flow impact on pipelines, Part I: Experimental investigation. *Coast. Eng.* 55 (12), 1209–1218.